

# Influence of external driving on decays in the geometry of the LiCN isomerization

Matthias Feldmaier,<sup>1</sup> Johannes Reiff,<sup>1</sup> Rosa M. Benito,<sup>2</sup> Florentino Borondo,<sup>3,4</sup> Jörg Main,<sup>1</sup> and Rigoberto Hernandez<sup>5,6, a)</sup>

<sup>1)</sup> *Institut für Theoretische Physik 1, Universität Stuttgart, 70550 Stuttgart, Germany*

<sup>2)</sup> *Grupo de Sistemas Complejos, Escuela Técnica Superior de Ingeniería Agronómica, Alimentaria y de Biosistemas, Universidad Politécnica de Madrid, 28040 Madrid, Spain*

<sup>3)</sup> *Instituto de Ciencias Matemáticas (ICMAT), Cantoblanco, 28049 Madrid, Spain*

<sup>4)</sup> *Departamento de Química, Universidad Autónoma de Madrid, Cantoblanco, 28049 Madrid, Spain*

<sup>5)</sup> *Department of Chemistry, Johns Hopkins University, Baltimore, Maryland 21218, USA*

<sup>6)</sup> *Departments of Chemical & Biomolecular Engineering, and Materials Science and Engineering, Johns Hopkins University, Baltimore, Maryland 21218, USA*

(Dated: 25 December 2021)

The framework of transition state theory relies on the determination of a geometric structure identifying reactivity. It replaces the laborious exercise of following many trajectories for a long time to provide chemical reaction rates and pathways. In this paper, recent advances in constructing this geometry even in time-dependent systems are applied to the  $\text{LiCN} \rightleftharpoons \text{LiNC}$  isomerization reaction, driven by an external field. We obtain decay rates of the reactant population close to the transition state by exploiting local properties of the dynamics of trajectories in and close to it. We find that the external driving has a large influence on these decay rates when compared to the non-driven isomerization reaction. This, in turn, provides renewed evidence for the possibility of controlling chemical reactions, like this one, through external time-dependent fields.

## I. INTRODUCTION

The motion of atoms in chemical reactions can often be described by classical mechanics on a Born-Oppenheimer potential separating reactants from products through a rank-1 saddle. The corresponding barrier has one unstable direction along the reaction coordinate, and the remaining orthogonal modes along the stable direction. The framework of transition state theory (TST) provides both a qualitative and quantitative description of reaction rates using the sum of the flux through a particular dividing surface (DS).<sup>1–7</sup> In the most naive case, the DS is a plane located at the saddle and parallel to the orthogonal modes, providing the usual qualitative, but not exact, Arrhenius-like rates.<sup>1,2,4,8,9</sup> More generally, the DS can be extended to a fully recrossing-free surface in phase space giving rise to exact rates.<sup>10–21</sup>

In the phase space associated with the barrier region of such systems, the most relevant object is the normally hyperbolic invariant manifold (NHIM),<sup>15,22–25</sup> which is a natural generalization of the time-independent two-dimensional periodic orbit dividing surface (PODS).<sup>3,4</sup> The NHIM contains all trajectories that are mathematically bound to the saddle forever and will, therefore, never leave either to the reactant or product sides. Hence, this intermediate structure lying between reactants and products is also often referred to as the transition state

(TS). In multidimensional autonomous Hamiltonian systems, the NHIM can be constructed approximately up to a desired order using normal form expansions,<sup>12,26–35</sup> or numerically by application up to desired accuracy of Lagrangian descriptors,<sup>24,25,36–38</sup> the binary contraction method,<sup>39</sup> and machine learning algorithms.<sup>25,40,41</sup> Many of these methods also allow for the construction of a time-dependent NHIM when the system is driven through time-dependent potentials. Given the NHIM, a DS can then be attached<sup>24,25,42,43</sup> to it in the sense that it is anchored (or rooted) at the NHIM and lifted vertically in the momentum space. The resulting time-dependent DS is recrossing-free, at least, in its local neighborhood. Such recent advances are necessary for us to address the challenge of a driven chemical reaction such as done here on LiCN through external coupling of its dipole moment.

The dynamics transverse to the NHIM is unstable. Hence, any trajectory having a small deviation from it will depart to either the reactant or the product side. This departure of trajectories in a close neighborhood of the NHIM is associated with a rate which describes the decay of reactant population close to the TS.<sup>44</sup> One approach for obtaining these decay rates in a driven reaction was pursued using Floquet exponents and demonstrated for a one-dimensional system.<sup>45</sup> In this model, the NHIM contains only a single trajectory—*viz.* the TS trajectory<sup>15,17,46</sup>—to which a DS can be attached. The decay rates obtained here correspond to the decay of the reactant population close to the TS in the sense of the usual flux that crosses it in the forward direction. We effectively impose absorbing boundary conditions by ne-

<sup>a)</sup>Correspondence to: r.hernandez@jhu.edu

glecting the long-time return of the trajectories after they have reached the product or reactant, and restrict our use of the term *global dynamics* to refer to all motion before its crossing of this boundary to product or reactants. Thus, in the limiting case that the DS is non-recrossing in this global sense, these decay rates are the forward reaction rates as was the case in the paradigmatic system of Ref. 45. To the extent, however, that the DS that we construct is *local*, then the decay rates are the direct rates associated to this particular barrier. When this barrier is rate determining, then this local decay is once again the overall rate. Even when it is not, the decay rate remains a useful quantity to describe the flow along the reaction pathway near an identified TS.

In multidimensional systems, infinitely many trajectories are located on the NHIM of a time-dependent driven barrier. Reactive trajectories may pierce the DS close to any of them. The full dynamics of bound trajectories inside the NHIM then needs to be considered when obtaining the decay rates of a reactant population close to the TS. This problem was recently addressed in Ref. 44 through three different approaches: (i) propagation of an appropriate ensemble of reactive trajectories and observing their piercing through the DS as a function of time, (ii) analysis of the structure of the stable and the unstable manifold close to the NHIM, or (iii) a multidimensional extension of the so-called Floquet method of Ref. 45 in which the Floquet exponents are used to obtain the decay rate. These approaches enabled the analysis of a two-dimensional model reaction with numerical precision.<sup>44</sup> It also confirmed that in a multidimensional system, the driving potential has a large influence on the dynamics of trajectories inside the NHIM and the corresponding decay of the reactant population close to the TS. The aim of this paper is the application of these methods to the case of a model with high fidelity to a real chemical system. Specifically, we address the (periodically driven)  $\text{LiCN} \rightleftharpoons \text{LiNC}$  isomerization reaction. The heavy mass of the Li allows us to consider this reaction in the classical limit, though there has been a lot of interest in the quantum versions of TST<sup>28,47,48</sup> which can be revealed in the case of the corresponding HCN reaction,<sup>49</sup> whose classical reaction geometry was also addressed previously in the time-independent case.<sup>50</sup> The important 1:2 resonance in that system<sup>51</sup> does not show up as strongly in the present LiCN system because of the difference in masses. This difference allows us to simplify the current analysis by constraining the CN vibration to be fixed.

For the LiCN isomerization reaction, analytical expressions for both the potential energy surface,<sup>52</sup> as well as for the dipole surface<sup>53</sup> are known. The  $\text{LiCN} \rightleftharpoons \text{LiNC}$  isomerization reaction has received significant attention in the literature—e.g., in molecular dynamics simulations of LiCN in an argon bath,<sup>54–57</sup> an analysis of the geometric structures underlying the LiCN reaction dynamics,<sup>58,59</sup> and as a paradigmatic example for the control of other reactions using external fields.<sup>60–62</sup> Here, we apply a periodically driven external field on

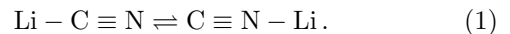
the molecule. This introduces a complexity not captured by the PODS in two-dimensional reactions because we now require a corresponding time-dependent DS to distinguish reactant and product regions, and it allows us to reveal the influence of driving on the phase-space resolved decay rates obtained for reactant populations close to the TS. These rates describe how trajectories deviate from the time-dependent NHIM—which is the multidimensional generalization of the TS-trajectory—in analogy to the characterization of the deviation from unstable periodic trajectories though the use of Lyapunov exponents.

The paper is organized as follows. In Sec. II A, the  $\text{LiCN} \rightleftharpoons \text{LiNC}$  isomerization reaction is introduced. The static and driven equations of motion in Secs. II A 1 and II A 2, respectively, are recapitulated using the known literature forms and parameters. Details of the theory and implementation of three different approaches<sup>44</sup> introduced recently for the numerical evaluation of the decay rates are included in the Supplementary Material. Because of their complementary advantages, each is used to numerically determine the decay rates of the reactant population close to the TS. Associated structures for the periodically driven  $\text{LiCN} \rightleftharpoons \text{LiNC}$  isomerization reaction are provided in Sec. III and compared with the corresponding results for the non-driven isomerization reaction. The dynamics of trajectories on the NHIM and the associated phase-space resolved decay rates are examined.

## II. THEORY AND METHODS

### A. Isomerization of LiCN

The three-atom molecule LiCN consists of carbon (C) and nitrogen (N) atoms forming a strongly bound cyanide anion which is weakly bound to the lithium (Li) cation regiospecifically. That is, it is an isomeric molecule with two stable conformations, LiCN and LiNC,



Its motion can be described quasi-classically in the Born-Oppenheimer approximation and analytical approximations for both the energy surface<sup>52</sup> and the dipole surface<sup>53</sup> are known from the literature. It can be represented in a body-fixed reference frame  $(x', z')$ , illustrated in Fig. 1 using Jacobi coordinates, where the  $z'$ -axis lies on the vector  $\mathbf{R}$  pointing from the center of mass of the cyanide towards the lithium atom. Here, the relative distance between the nitrogen and the carbon atom is labeled  $r_{\text{CN}}$  and the angle between  $\mathbf{R}$  and  $\mathbf{r}_{\text{CN}}$  is referred to as  $\vartheta = \angle(\mathbf{R}, \mathbf{r}_{\text{CN}})$ . Consequently, the regions near  $\vartheta = 0$  and  $\vartheta = \pi$  correspond to the LiCN and LiNC isomers, respectively. When described in a body-fixed reference frame the angle  $\alpha = \angle(\hat{\mathbf{e}}_z, \mathbf{R})$  yields the overall orientation of the molecule relative to a space-fixed coordinate system  $(x, z)$  as also indicated in Fig. 1. Here,

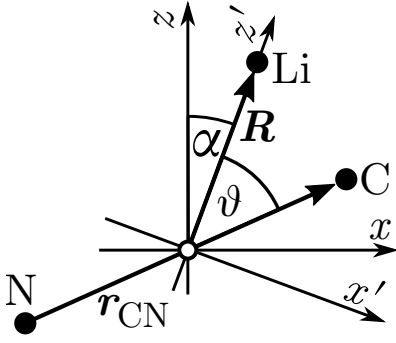


FIG. 1. Coordinate description of the  $\text{LiCN} \rightleftharpoons \text{LiNC}$  isomerization reaction. The vector  $\mathbf{R}$  connects the center of mass of cyanide (CN) with the lithium atom (Li) and the relative distance between the carbon (C) and the nitrogen atom (N) is denoted as  $\mathbf{r}_{\text{CN}}$ . The angle between  $\mathbf{R}$  and  $\mathbf{r}_{\text{CN}}$  is labeled  $\vartheta$ . A body-fixed coordinate system  $(x', z')$  is attached to the center of mass of the cyanide with the  $z'$ -axis along the direction of  $\mathbf{R}$ . An additional angle  $\alpha$  is introduced between the  $z$ -axis of a space-fixed coordinate system  $(x, z)$  and the vector  $\mathbf{R}$  (and therefore the  $z'$ -direction of the body-fixed reference frame). It describes the possible rotation of the LiCN molecule within the  $(x, z)$  plane.

$\hat{\mathbf{e}}_z$  is the unit vector in the  $z$ -direction of the space-fixed coordinate system.

### 1. Non-driven isomerization reaction

In the absence of time-dependent external fields, the energy is conserved in the isomerization process and the corresponding potential energy surface of the non-driven  $\text{LiCN} \rightleftharpoons \text{LiNC}$  isomerization reaction is independent of the overall orientation  $\alpha$  of the molecule. It can be approximated by a potential energy surface  $V(R, \vartheta)$  that only depends on  $R = |\mathbf{R}|$  and  $\vartheta$ , i.e., the intrinsic degrees of freedom of the molecule. The bond distance of the cyanide anion is held fixed at  $|\mathbf{r}_{\text{CN}}| = 2.186 a_0$  with  $a_0$  being the Bohr radius, in keeping with earlier work showing that it has little effect on the dynamics.<sup>63–65</sup>

We use the potential energy surface  $V(R, \vartheta)$  of Ref. 52 for our calculations. As shown in Fig. 2 (a), there exist two local minima on the energy surface corresponding to the linear structures LiCN ( $\vartheta = 0$ ) and LiNC ( $\vartheta = \pi$ ). In between these two minima, at  $\vartheta = 0.292\pi$ , a rank-1 saddle represents the bottleneck of the isomerization reaction, visualized by the equipotential lines in Fig. 2 (a). At the energies above the barrier typical for reaction, the motion of the Li atom between the isomers appears as orbits around the cyanide.

The corresponding *classical rotationless two degrees of freedom Hamiltonian*, as applied to the LiCN reaction,<sup>58,65</sup> is

$$\mathcal{H} = \frac{p_R^2}{2\mu_1} + \frac{1}{2} \left( \frac{1}{\mu_1 R^2} + \frac{1}{\mu_2 r_e^2} \right) p_\vartheta^2 + V(R, \vartheta), \quad (2)$$

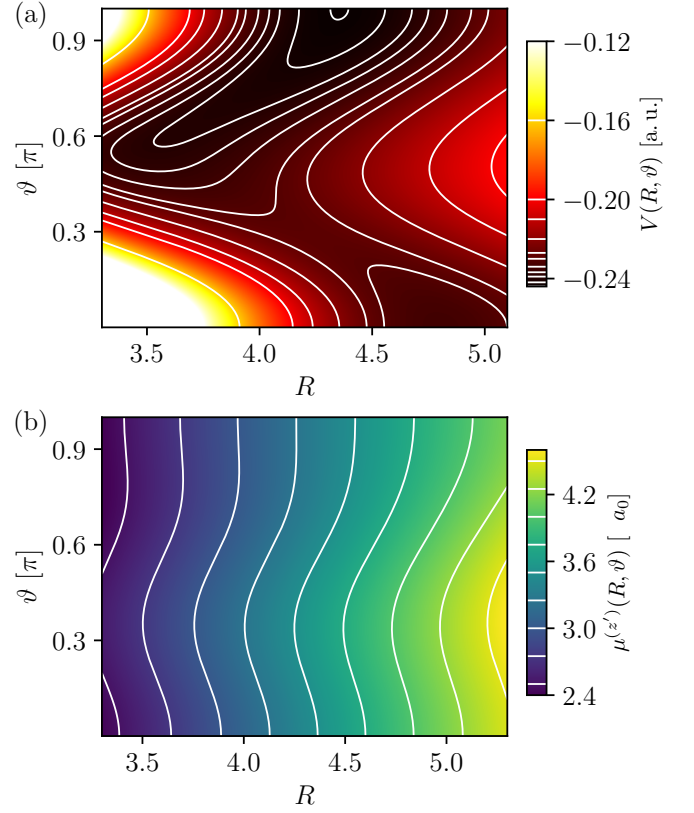


FIG. 2. (a) The potential energy surface  $V(R, \vartheta)$  in Eq. (2) for the LiCN isomerization reaction taken from Ref. 52. The two stable conformations of LiCN at  $\vartheta = 0$  and LiNC at  $\vartheta = \pi$  are separated by a rank-1 saddle. (b) The  $\mu^{(z')}(R, \vartheta)$  part of the dipole surface according to Eq. (6). The corresponding analytical form is taken from Ref. 53.

under the assumption that the canonical momentum  $p_\alpha = 0$  is fixed for non-rotating molecules. Using Hamilton's formalism, the dynamics of the  $\text{LiCN} \rightleftharpoons \text{LiNC}$  isomerization reaction in the absence of external fields can be obtained for the state  $\gamma(t) = (\vartheta, p_\vartheta, R, p_R)^T$  by numerically integrating a set of first order differential equations for  $\dot{\gamma}(t)$ , i.e.

$$\dot{\vartheta} = \left( \frac{1}{\mu_1 R^2} + \frac{1}{\mu_2 r_e^2} \right) p_\vartheta, \quad (3a)$$

$$\dot{p}_\vartheta = -\frac{dV(R, \vartheta)}{d\vartheta}, \quad (3b)$$

$$\dot{R} = \frac{p_R}{\mu_1}, \quad (3c)$$

$$\dot{p}_R = \frac{p_\vartheta^2}{\mu_1 R^3} - \frac{dV(R, \vartheta)}{dR}. \quad (3d)$$

In the present work, we adopt a fourth order Runge-Kutta algorithm with a fixed step size.<sup>66</sup> The first derivatives of the potential in Eqs. (3) have been implemented analytically in C++.<sup>67</sup>

## 2. Driven isomerization reaction

The aim of this work is to reveal how external driving influences the decay rates of the reactant population close to the transition state (TS). Such external driving can be induced by a time-dependent homogeneous electric field along a fixed direction. We call this the  $z$  direction, and write the driving term as

$$\mathbf{E}(t) = E_0 \sin(\omega t) \hat{\mathbf{e}}_z, \quad (4)$$

which couples to the molecule's dipole moment  $\boldsymbol{\mu}$ . This makes the Hamiltonian of Eq. (3) time-dependent through the added term

$$V_{\text{dip}}(t) = -\boldsymbol{\mu} \cdot \mathbf{E}(t) \quad (5)$$

to the potential energy.<sup>68</sup> To complete the equations, however, we must now also specify a continuous representation for the molecule's dipole moment  $\boldsymbol{\mu}$ , the so-called *dipole surface*, accounting for the fact that the underlying electronic wave functions vary as a function of the Born-Oppenheimer coordinates.

Individual points of the dipole surface have earlier been obtained using SCF methods.<sup>52</sup> Motivated by the success of Wormer and co-workers<sup>52,64</sup> in representing the SCF potential energy surface, Brocks *et al.*<sup>53</sup> constructed analytical expressions ( $\mu^{(x')}(R, \vartheta)$ ,  $\mu^{(z')}(R, \vartheta)$ ) for the dipole moment of LiCN in the body-fixed reference frame (see Fig. 1). We use this dipole surface with the corrections involving sign errors, noted recently by Borondo and coworkers.<sup>62</sup> The  $z'$ -part of this dipole surface, which is at least 15 times larger than the dipole moment  $\mu^{(x')}$  in the  $x'$ -direction, is shown in Fig. 2 (b). The body-fixed and space-fixed coordinate systems differ by a rotation with angle  $\alpha$ , and thus the dipole moment in the space-fixed coordinate system reads

$$\boldsymbol{\mu}(R, \vartheta, \alpha) = \begin{pmatrix} \cos \alpha & \sin \alpha \\ -\sin \alpha & \cos \alpha \end{pmatrix} \begin{pmatrix} \mu^{(x')}(R, \vartheta) \\ \mu^{(z')}(R, \vartheta) \end{pmatrix}. \quad (6)$$

Neglecting the small component  $\mu^{(x')}(R, \vartheta)$  in Eq. (5) the dipole potential now reads

$$V_{\text{dip}}(R, \vartheta, \alpha, t) \approx -E_0 \sin(\omega t) \mu^{(z')}(R, \vartheta) \cos \alpha. \quad (7)$$

We then further approximate  $\cos \alpha \approx 1$  removing the corrections from the oscillations in  $\alpha$  around the minimum at  $\alpha = 0$ , and allowing us to reduce the dimensionality to only the two remaining degrees of freedom,  $R$  and  $\vartheta$ . Although we have not fully explored the most general conditions for which this approximation will be valid, at the very least they will be satisfied when the oscillations in  $\alpha$  are faster than the other motion. In this limit, the potential on  $(R, \vartheta)$  results from the effective field obtained from the average over  $\alpha$ , and reduces to a form with a renormalized prefactor,  $E_0$ , and no  $\alpha$  dependence. We can thus focus on the reduced-dimensional Hamiltonian

$$\mathcal{H}_{\text{driven}}(R, \vartheta, t) = \mathcal{H} + V_{\text{dip}}(R, \vartheta, t), \quad (8)$$

where  $\mathcal{H}$  is the non-driven Hamiltonian of Eq. (2) and the time-dependent driving is included via the dipole potential

$$V_{\text{dip}}(R, \vartheta, t) = -E_0 \mu^{(z')}(R, \vartheta) \sin(\omega t). \quad (9)$$

The equations of motion take the same form as for the non-driven case given in Eqs. (3) with  $V$  replaced by the (time-dependent) potential

$$V_{\text{driven}}(R, \vartheta, t) = V(R, \vartheta) + V_{\text{dip}}(R, \vartheta, t). \quad (10)$$

Again, solutions are found numerically using a fourth order Runge-Kutta algorithm<sup>66</sup> and a C++ implementation of the derivatives of  $V_{\text{driven}}$  with respect to  $R$  and  $\vartheta$ .

## III. RESULTS AND DISCUSSION

The relative movement of individual atoms in the non-driven  $\text{LiCN} \rightleftharpoons \text{LiNC}$  isomerization reaction is described by trajectories obtained via the propagation of an initial state according to Eq. (3). The evolving state is identifiable as *reactant*  $\mathcal{R}$  if  $\vartheta < 0.15\pi$  and *product*  $\mathcal{P}$  if  $\vartheta > 0.5\pi$  when it is found in the corresponding regions highlighted in Fig. 3 (a). The contours of the potential are also shown, providing a view of the underlying channel for trajectories to go between  $\mathcal{R}$  and  $\mathcal{P}$ .

In Fig. 3 (a), representative trajectories are initialized at  $(R = 4.3, p_R = 0)$  for four different combinations of  $\vartheta$  and  $p_\vartheta$  as also highlighted by the corresponding marker in Fig. 3 (b). Each full trajectory, displayed with a different line style, is obtained by propagating the initial point in phase space according to Eqs. (3) forward and backward in time until the reactant or the product state is reached. Two of these trajectories are reactive (thick solid green with initial circle, thin dashed white with initial square) and the other two (thin solid yellow with initial triangle, thin dashed purple with initial diamond) are not since their energy is too low to cross the barrier.

The shaded regions of Fig. 3 (b) label the reactive ( $\mathcal{R} \rightarrow \mathcal{P}$  and  $\mathcal{P} \rightarrow \mathcal{R}$ ) and non-reactive ( $\mathcal{R} \rightarrow \mathcal{R}$  and  $\mathcal{P} \rightarrow \mathcal{P}$ ) initial points in the  $(\vartheta, p_\vartheta)$  subspace. These regions are separated by the stable and the unstable manifolds which intersect at a particular point  $(\vartheta, p_\vartheta)^{\text{NHIM}}$  of the NHIM for  $(R = 4.3, p_R = 0)$ . The white dashed square trajectory is initialized closest to one of the manifolds and stays in the barrier region for nearly three oscillations in the stable direction of the barrier. Hence, it crosses a corresponding dividing surface (DS) separating reactants from products closest to the normally hyperbolic invariant manifold (NHIM). While the structures illustrated in Fig. 3 were previously seen in a generic model system with a driven rank-1 saddle,<sup>24,25,39,44</sup> the results here show that they are realized also in a specific model of a chemical reaction. In both cases, the geometry is described by the stable and unstable manifolds of the barrier, and the nature of the reactivity is determined by the associated DS attached to the NHIM.

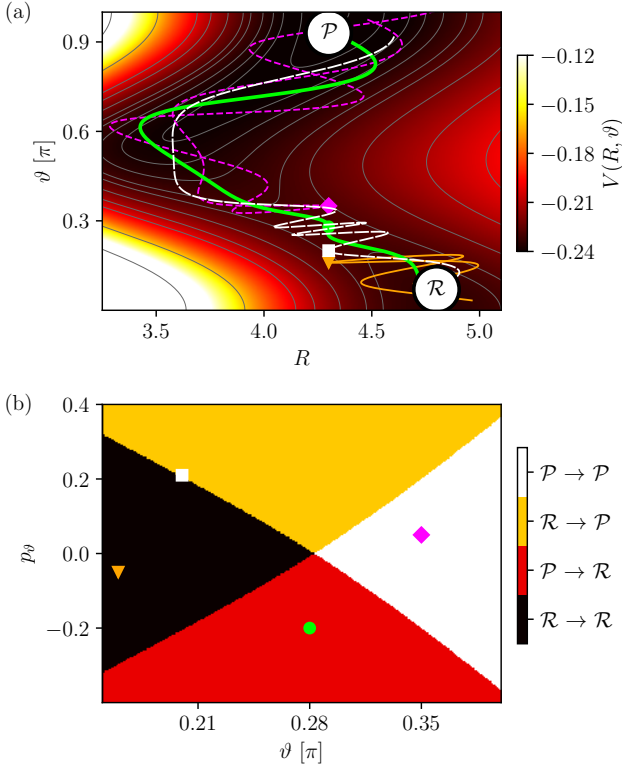


FIG. 3. Reactive and non-reactive behavior of trajectories initially launched close to the barrier region (illustrated with individual markers), and propagated according to Eqs. (3) forward and backward in time until the reactant  $\mathcal{R}$  or product  $\mathcal{P}$  state is reached. (a)  $(R, \vartheta)$  position space representation with the potential energy surface according to Fig. 2 (a) as shown in color (or shading in print) defined by the bar to its right. (b)  $(\vartheta, p_\vartheta)$  cross-section of the phase space with the reactive and non-reactive regions encoded in color (or shading in print) defined by the bar to its right. For all trajectories, the remaining coordinate  $p_R$  is initially set to zero.

#### A. Dynamics of periodically driven transition states

When periodically driving the  $\text{LiCN} \rightleftharpoons \text{LiNC}$  isomerization reaction, the potential  $V_{\text{dip}}(R, \vartheta, t)$  in Eq. (9) is explicitly time-dependent and the energy of the system is no longer conserved. Still, a two-dimensional NHIM exists in the barrier region, which contains all trajectories that never leave this region, neither forward, nor backward in time. In contrast to a static system, however, the NHIM becomes time-dependent. For periodic driving, such a NHIM oscillates with the same frequency as that of the driving of the barrier because of the symmetry of the system with respect to time.

The Poincaré surface of section (PSOS) is a useful tool for resolving the dynamics of this time-dependent NHIM in a periodically driven system. Therein, the positions  $(R, p_R)$  of several trajectories on the NHIM are marked after integer multiples of the driving period for a time much longer than a single period of the exter-

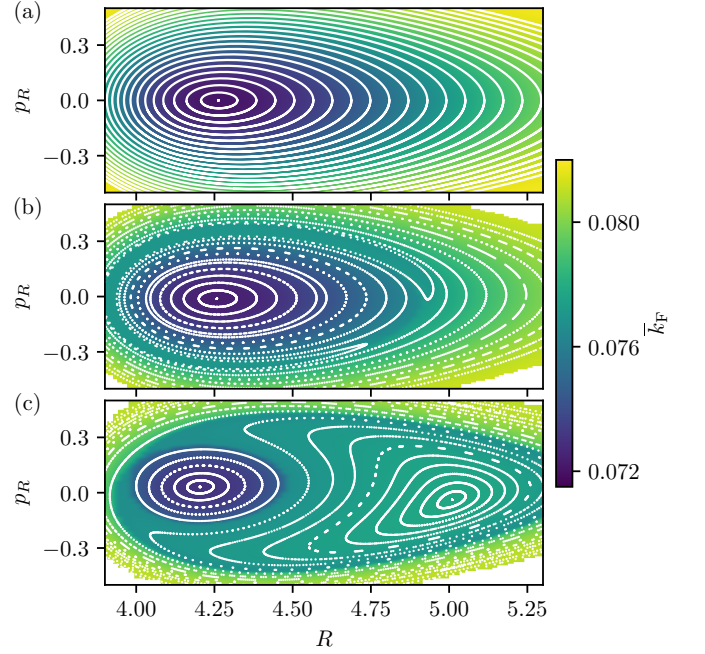


FIG. 4. The stable structures obtained from the dynamics on the NHIM are compared to Floquet rates  $\bar{k}_F$  for the decay of trajectories from the NHIM for the static (a) and the driven LiCN isomerization reaction with  $E_0 = 0.01$  and  $\omega = 0.01\pi$  in (b) and  $\omega = 0.02\pi$  in (c), respectively. The white curves in all three panels are the PSOSs obtained from periodic orbits in (a), and from the propagation of trajectories for 400 periods of the external driving while marking their instantaneous position  $(R, p_R)$  after each period in (b) and (c). The color encoding shows the mean Floquet rates obtained for  $100 \times 100$  stabilized trajectories which are initialized on an equidistant grid for the ranges of  $R \in [3.8, 5.3]$  and  $p_R \in [-0.5, 0.5]$  on the NHIM. Its contours (not shown but indicated through the color variation) coincide with the PSOSs. All trajectories are stabilized to the NHIM using the BCM with a tolerance of  $10^{-12}$  and the colors are interpolated using bicubic splines.

nal driving. When propagating trajectories for such a relatively long time, the instability of the dynamics in the NHIM can become problematic as errors produced by any numerical propagator are exponentially increasing. Consequently, trajectories initialized as precisely as possible in the NHIM nevertheless “fall down” from the barrier to either the reactant or the product side. This problem can be addressed through the use of a stabilized propagator,<sup>41,44</sup> which successively projects unstable trajectories back into the NHIM after an appropriately chosen time step using the binary contraction method (BCM).

In the static case according to Eq. (2), the energy is conserved, so each trajectory in Fig. 4 (a) is periodic. The central fixed point corresponds to the trajectory resting at the saddle point of the barrier—*viz.* at  $R = 4.2626$  and  $\vartheta = 0.2800\pi$ . The frequency of oscillations in the stable direction of the static barrier decreases monotonously from about  $\omega_{\text{orth}} = 0.043\pi$  for the trajectories close to



the fixed point to, e.g., about  $\omega_{\text{orth}} = 0.035\pi$  for a trajectory with energy  $E = -0.19$ . The driving frequencies, chosen below, range between 2 to 4 times slower than the oscillation frequencies of the orthogonal modes and thus provide a non-trivial perturbation to the system. The PSOs at these driving frequencies indeed show significant changes compared to the static case as shown in Fig. 4.

For the driven systems, the stabilized trajectories are initiated on the NHIM at  $t_0 = 0$ . They are propagated for 400 periods of the external driving with amplitude  $E_0 = 0.01$  and frequency  $\omega = 0.01\pi$ . Specifically, the values are chosen to correspond to an electromagnetic field with frequency 4.85 THz (wavelength  $\lambda = 61.9\mu\text{m}$ )<sup>69</sup> and amplitude  $E_0 = 5.14 \times 10^7 \text{ V cm}^{-1}$ . After each period of  $T = 200$ , the instantaneous position  $(R, p_R)$  of each trajectory in the NHIM is marked. The stabilization of each trajectory into the NHIM was performed using the BCM with an error tolerance of  $10^{-12}$ . Finally, we observe that the PSOs for the driving cases look quite different from the static case because the driven NHIM is time-dependent.

The driven trajectories are generally no longer periodic and energy is not conserved, leading to a more complex geometric structure. Nevertheless, at first glance, the structure of the trajectories of the driven barrier in Fig. 4 (b) looks very similar to those of the non-driven barrier in Fig. 4 (a) having a central fixed point and tori (trajectories in the non-driven case) around it. On the right-hand side of Fig. 4 (b) at about  $R = 4.8$  and  $p_R = -0.2$ , an unstable fixed point is visible, interruption the regular arrangement of the tori. According to the Poincaré-Birkhoff theorem,<sup>70</sup> only an even number of fixed points may occur in a perturbed system (if regarded not precisely at the bifurcation values), and consequently, the appearance of the unstable fixed point is accompanied by the emergence of a stable fixed point. The latter is located approximately at  $R = 3.9$  and  $p_R = 0$  and is not directly visible here.

To magnify the influence of the moving barrier, the PSOs in Fig. 4 (c) is obtained in the same way as in Fig. 4 (b) but with twice the frequency of the external driving  $\omega = 0.02\pi$ . Physically, this corresponds to an electromagnetic field with frequency 9.70 THz (wavelength  $\lambda = 30.9\mu\text{m}$ ).<sup>69</sup> Now, the external driving has a strong impact on the dynamics of the trajectories on the NHIM. An additional unstable and an additional stable fixed point are clearly visible. Both stable fixed points belong to separate period-1 trajectories, that are encircled by many quasi-periodic trajectories on various tori. These structures, not seen in the non-driven barrier and only partially seen with weak driving, arise solely due to the external driving.

A three-dimensional representation  $(R, \vartheta, p_R)$  of the three periodic trajectories corresponding to the stable fixed points clearly shown in Fig. 4 (b) and (c) is given in Fig. 5 (a). Here, the inner trajectory, corresponding to the visible stable fixed point in Fig. 4 (b) at initial posi-

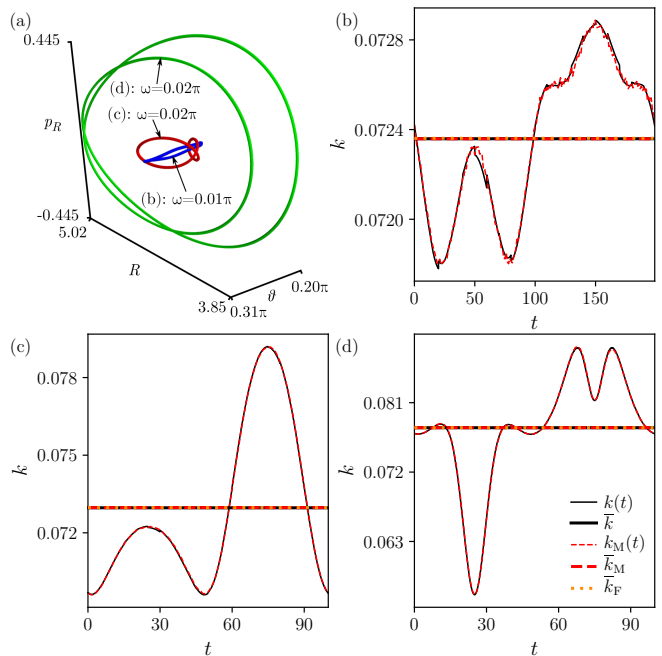


FIG. 5. (a) Representation  $(R, \vartheta, p_R)$  of period-1 trajectories on the NHIM of the driven LiCN isomerization reaction. The inner trajectory corresponds to the central elliptic fixed point in Fig. 4 (b), the intermediate and outer double-loop trajectories to the elliptic fixed points in Figs. 4 (c) and 4 (d) at positions  $R \approx 4.2$  and  $R \approx 5.0$ , respectively. Parts (b)-(d) show the instantaneous ensemble rate  $k(t)$  (thin black line), the time-averaged mean ensemble rate  $\bar{k}$  (thick black horizontal line), the mean Floquet rate  $\bar{k}_F$  (orange dotted horizontal line), the instantaneous manifold rate  $k_M(t)$  (thin red dashed line), and the time-averaged mean manifold rate  $\bar{k}_M$  (thick red horizontal dashed line). The methods for obtaining these various rates are described in the supplementary material.

tion  $R = 4.2579$  and  $p_R = -0.0117$  shows just very little movement in the stable direction of the barrier. However, the trajectory in between, corresponding to the stable fixed point at  $R = 4.2040$  and  $p_R = 0.0313$  and especially the outer trajectory, corresponding to the stable fixed point at  $R = 5.0096$  and  $p_R = -0.0378$  of Fig. 4 (c) are subject to significant movement in the stable direction of the barrier. Note, that these two trajectories show two oscillations in direction of the orthogonal mode of the barrier although they are both period-1 trajectories with respect to the external driving.

## B. Instantaneous decay near periodic trajectories on the driven NHIM

Using the methods introduced in Ref. 44 and discussed as supplementary material, the instantaneous reactant decay rates associated with trajectories on the driven NHIM can be obtained. First, we analyze the three period-1 trajectories displayed in Fig. 5 (a). The inner trajectory—shown in blue (in color) on the (a) panel—

is obtained for a driving frequency of  $\omega = 0.01\pi$ , while the two outer trajectories—shown in blue and green (in color) on the (a) panel—are obtained for a system with a larger driving frequency of  $\omega = 0.02\pi$ , as labeled.

Figure 5 (b) presents the instantaneous decay rates associated with trajectories close to the inner period-1 trajectory with an initial point  $R = 4.2579$  and  $p_R = -0.0117$  at time  $t = 0$  on the NHIM of a driven barrier with  $E_0 = 0.01$  and  $\omega = 0.01\pi$ . To obtain decay rates with the ensemble method, the trajectory is divided into 20 segments. For each segment, an ensemble of 200 reactive trajectories is initialized close to the NHIM with a distance of  $\Delta\vartheta = 10^{-3}$ . Patching together these individual segments yields the thin black line in Fig. 5 (b). The corresponding mean ensemble decay rate is obtained by averaging over a full period of the external driving, yielding  $\bar{k} = 0.0724$  and displayed as a thick solid vertical line. This result can be verified using the Floquet method, see supplementary material, which yields a mean Floquet rate of  $\bar{k}_F = 0.0724$  for this trajectory. This mean Floquet rate, shown as an orange dotted vertical line in Fig. 5 (b), is in perfect agreement with the mean ensemble rate. Using the local manifold analysis (LMA), see supplementary material, a third verification of these decay rates can be obtained. The thin red dashed line in Fig. 5 (b) marks the instantaneous manifold rate  $k_M(t)$  and the thick red dashed vertical line marks the mean manifold rate  $\bar{k}_M = 0.0724$ , averaged over a full period of the external driving. Both lines fit the results of the other two methods.

The same procedure used to obtain Fig. 5 (b) is repeated for the two remaining trajectories of Fig. 5 (a). Figures 5 (c) and 5 (d) present the results for the intermediate trajectory (labeled c, and red in color), and the outer trajectory (labeled d, and green in color) in Fig. 5 (a), respectively. In both cases, the instantaneous decay rates obtained via the LMA correspond perfectly to the instantaneous decay rates of the ensemble method, and their mean rates are also in perfect agreement with the obtained Floquet rates. Hence,  $\bar{k} = \bar{k}_M = \bar{k}_F = 0.0730$  for the intermediate trajectory, and  $\bar{k} = \bar{k}_M = \bar{k}_F = 0.0778$  for the outer trajectory.

The decay of the reactant population close to the three different period-1 trajectories in Figs. 5 (b)-(d) is represented by very different instantaneous rates, and consequently also mean rates. In addition, the amount of variation of the instantaneous rates varies strongly for each trajectory. For the inner trajectory that according to Fig. 5 (a) has the smallest movement in the orthogonal mode, the relative change of the instantaneous rate,  $\Delta k \approx 10^{-3}$ , is very small. Consequently, the effect of the external driving is barely noticeable. The intermediate trajectory of Fig. 5 (a) has significantly more motion in the stable direction of the barrier. The relative change,  $\Delta k \approx 10^{-2}$ , of the instantaneous rate is considerably larger as seen in Fig. 5 (c). The outer trajectory of Fig. 5 (a) has by far the largest movement in the stable direction of the barrier. The relative change,

$\Delta k \approx 0.5 \times 10^{-1}$ , in the instantaneous rates in Fig. 5 (d) is also the largest. Thus, we can conclude that the influence of the external driving is high if a trajectory has significant motion in the direction of the orthogonal modes. Further evidence for this effect follows in Sec. III C in the context of the decay rates associated with the numerous quasi-periodic trajectories on the driven NHIM.

### C. Phase-space resolved decay rates

We now obtain the phase-space resolved decay rates of the reactant population close to arbitrary trajectories on the NHIM of the periodically driven  $\text{LiCN} \rightleftharpoons \text{LiNC}$  isomerization reaction. As seen above, all three methods to calculate the decay of reactant population close to the transition state (TS) result in the same values for a specific period-1 trajectory, and hence we choose only one of these for the present calculation. Namely, the Floquet method is employed because it is relatively easy to implement and computationally fast to evaluate.

In all the cases of Fig. 4, the Floquet rates are overlaid on top of the PSOSs. They are obtained on equidistant grids using approximately 10 000 stabilized trajectories, and they are displayed through a shaded (or colored in color) encoding. All trajectories are propagated for a total time up to  $t = 10\,000$  as needed to converge. The individual Floquet rates are interpolated using bicubic splines to smooth the discrete points. We found that the decay rates of all the trajectories located on the corresponding regular tori are indeed the same. This is expected since any quasi-periodic trajectory on such a torus in general covers it in full if propagated for long enough. Thus, a unique decay rate is associated with each torus. This observation is true for the static system using a simpler argument. Namely, the Floquet rate reduces to a property of any of the periodic trajectories on the static NHIM because the tori is necessarily periodic.

When comparing the obtained mean Floquet rates of the driven system with  $E_0 = 0.01$  and  $\omega = 0.01\pi$  in Fig. 4 (b) to the mean Floquet rates of the static system according to Fig. 4 (a), the influence of the external driving is small. In Fig. 4 (b), the mean Floquet rate obtained at the clearly visible elliptic fixed point in the center of the tori corresponds to the rates already obtained in Fig. 5 (b) with all three methods introduced in Ref. 44 and provided as supplementary material. In the two cases of Fig. 4 (a) and Fig. 4 (b), the mean Floquet rates at the central fixed point are similar—that is, they are  $\bar{k}_F = 0.0721$  and  $\bar{k}_F = 0.0724$ , respectively. The primary difference is the emergence of structure that is barely visible here but more clearly visible in Fig. 4 (c) as discussed below.

A further increase in the frequency of the external driving to  $\omega = 0.02\pi$  leads to a drastic change in the structure as shown in Fig. 4 (c). Two clearly separated elliptical fixed points are now visible in the PSOS with each encircled by an individual set of tori dividing the NHIM

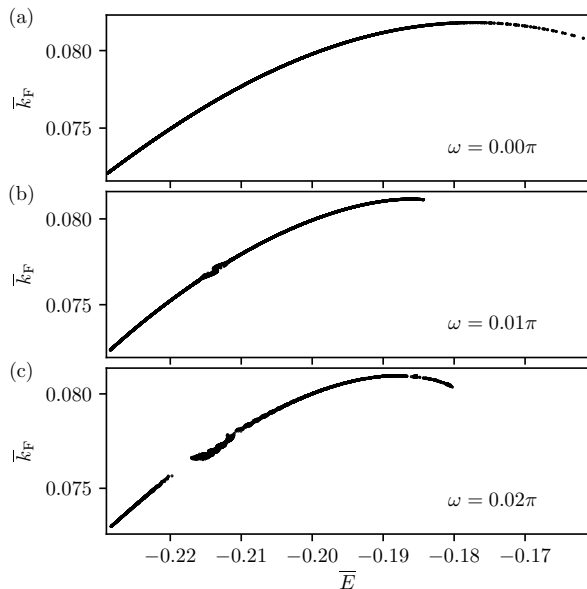


FIG. 6. The quantitative relation of the Floquet rates  $\bar{k}_F$  to the mean energies  $\bar{E}$  of trajectories on the NHIM obtained at three different driving frequencies  $\omega$  equal to  $0.00\pi$ ,  $0.01\pi$  and  $0.02\pi$  are shown in panels (a), (b) and (c), respectively. Each rate corresponds to a torus in Fig. 4 at the mean energy  $\bar{E}$ .

into two regions of very different Floquet rates. This means that two regions of very different stability emerge on the periodically driven NHIM. In the surrounding of the fixed point at  $R = 4.2040$  and  $p_R = 0.0313$ , the decay rates of the reactant population are rather small and approximately correspond to the mean Floquet rate of  $\bar{k}_F = 0.0730$  obtained for the central period-1 trajectory according to Fig. 5 (c). On the other hand, the mean Floquet rates in a region near the fixed point at  $R = 5.0096$  and  $p_R = -0.0378$  are rather large and approximately correspond to the mean Floquet rate  $\bar{k}_F = 0.0778$  of the associated central period-1 trajectory according to Fig. 5 (d).

For a periodically driven system, the instantaneous energy  $E(t)$  of trajectories in the NHIM is not conserved. However, by averaging the instantaneous and non-conserved energy of a given trajectory over many oscillations of the periodic driving, the mean energy  $\bar{E}$  of a specific torus is well defined and characteristic of the trajectory and its associated initial condition. The quantitative correspondence between the mean energy of a trajectory and the Floquet rate is revealed in Fig. 6 by plotting the Floquet rates obtained in Fig. 4 with respect to the corresponding (mean) energies of the trajectories.

As a control for the driven cases, Fig. 6 (a) shows the relation between the Floquet rate and the mean energy for the non-driven system of Fig. 4 (a). In this limit, energy is conserved. Thus the mean energy  $\bar{E}$  corresponds to the instantaneous energy  $E(t)$  of the respective trajectories. According to Fig. 6 (a), the relation between the energy and the Floquet rate in the static case

is not monotonic and has a maximum at approximately  $E = -0.18$ . A further increase of the energy of trajectories on the NHIM goes together with a decrease in the corresponding decay rate of the reactant population close to the TS. However, a maximum in these decay rates is associated with a minimum in the stability of the activated complex close to the TS. According to Fig. 6 (a), there seems to be a lower bound for the stability of this activated complex in the non-driven LiCN isomerization reaction.

The results for the driven system in Figs. 6 (b) for  $\omega = 0.01\pi$  and in Fig. 6 (c) for  $\omega = 0.02\pi$  correspond to cases in Fig. 4 (b) and (c), respectively. Despite the driving, they retain some similarity with the static case of Fig. 6 (a). Again, the relation between the Floquet rate of a trajectory on a given torus and the associated mean energy is non-monotonic and there seems to exist a maximum decay rate for the reactant population associated with trajectories on the NHIM.

In contrast to the static case, however, for the driven barrier case with  $\omega = 0.02\pi$ , a significant gap arises in the curve of Fig. 6 (c) at about  $\bar{E} = -0.22$ . This gap corresponds exactly to the emergence of tori around distinct fixed points seen in Fig. 4 (c). At the beginning of the upper edge of the gap in Fig. 6 (c), the curve initially fluctuates before becoming smooth again with increasing mean energy. The origin of this behavior is numerical because the Floquet method for non-periodic trajectories is defined only in the limit  $t \rightarrow \infty$  (see supplementary material). However, trajectories in Fig. 4 (c) are necessarily propagated for a finite time, and this leads to errors in the calculated Floquet rates which are small and appear as fluctuations. In other words, close to the boundary between the two regions of the different decay rates on the driven NHIM, the circulation times of quasi-periodic trajectories on the regular tori increases and longer propagation times are necessary to obtain a desired accuracy using the Floquet method. This behavior can also be seen in Fig. 6 (b) for the case with a driving frequency of  $\omega = 0.01\pi$ . A second stable fixed point is barely visible in Fig. 4 (b). Consequently, nearly no gap appears in Fig. 6 (b). Nevertheless, fluctuations are visible at the energy of the indicated fixed point on the left-hand side of Fig. 4 (b), and, hence, a gap is just emerging there.

#### IV. CONCLUSION AND OUTLOOK

In this paper, we study the influence of a periodically oscillating external field on the  $\text{LiCN} \rightleftharpoons \text{LiNC}$  isomerization reaction. In the static case, the energy is conserved and all trajectories on the associated normally hyperbolic invariant manifold (NHIM) are periodic. For a periodically driven system, nearly all trajectories contained in the NHIM are quasi-periodic and located on stable tori. The dynamics on the driven NHIM has been revealed by means of a Poincaré surface of section (PSOS). Depending on the frequency of the external field, a new set of



tori around a second stable fixed point emerges on the NHIM.

The associated mean decay rates of reactant population in a close neighborhood of the periodic or quasi-periodic trajectories on the NHIM are obtained by various methods.<sup>44</sup> Both in the static and driven cases, the decay rates differ significantly across these neighborhoods, and are approximately prescribed by the mean decay rates associated to the corresponding central periodic trajectory. The instantaneous decay rates for these central trajectories are also sensitive to the driving. Specifically, the relation between the mean decay rates associated with a specific torus and the corresponding mean energy of trajectories on this torus is non-trivial. There are two clearly distinguished regions associated with different mean decay rates of the reactant population close to the transition state (TS). They are approximately prescribed by period-1 trajectories identified at the center of the corresponding tori of the PSOS. They are consequently not continuously connected and a significant gap between the corresponding decay rate emerges. The regularity of the structure of the PSOS for the trajectories near the NHIM is not chaotic as one might have expected given the recently observed chaotic sea in the global phase space.<sup>71</sup> This points to the simplification arising from considering decay rates in the local neighborhood of the TS. Future work to extend these decay rates to the global rates thus needs to consider not just the possibility of additional barrier regions but also the complex dynamics that can arise from chaotic regions.

Thus the influence of the periodic external driving on the  $\text{LiCN} \rightleftharpoons \text{LiNC}$  isomerization reaction is large when compared to the static problem. Indeed, the emergence of different regions of the reactant population decay for the driven  $\text{LiCN} \rightleftharpoons \text{LiNC}$  isomerization reaction as well as the existence of gaps in both energy and decay rate between these separate regions are effects solely invoked by the external driving.

The possible effects from our approximate simplification of the  $\text{LiCN} \rightleftharpoons \text{LiNC}$  isomerization reaction to a body-fixed axes may need to be addressed. This would allow the molecules to rotate with respect to the external field and increase the dimensionality of the coordinate space of the problem beyond the two-dimensional case considered here. However, there is precedent from the earlier work of Ref. 62 that the reaction is much faster than the rotation and hence such effects are small. One could also include a Langevin-type description of the dynamics—according to, e.g., Ref. 57—to address the effects on the decay rates from a solvent as represented by the inclusion of both noise and friction. Alternatively, the effects on the decay rates from an all-atom solvent can be uncovered by inferring the stability of the NHIM from molecular dynamics trajectories. For example, the position of reactive trajectories across the dividing surface (DS) can be tracked simulations of  $\text{LiCN}$  in an argon bath such as those of Refs. 54–57. Applying an appropriate external driving could shift these reaction positions

to different regions of the NHIM and increases the reaction rate. From the results of the current work, we would expect that there would once again emerge different regions in the PSOS and the corresponding reactant decay rates which should be interpretable as reactive channels. When applying an appropriate external field a second and faster reactive channel with higher decay rates opens up and might serve to an increase of the reaction rate.

## SUPPLEMENTARY MATERIAL

In the supplementary material, we provide a detailed description of the methods used in the primary text. We summarize the details for the implementation of three approaches in determining the decay rates: Floquet analysis, ensemble method, and the local manifold analysis. We also present a technical derivation of the last of these methods.

## ACKNOWLEDGMENTS

The German portion of this collaborative work was supported by Deutsche Forschungsgemeinschaft (DFG) through Grant No. MA1639/14-1. RH's contribution to this work was supported by the National Science Foundation (NSF) through Grant No. CHE-1700749. M.F. is grateful for support from the Landesgraduiertenförderung of the Land Baden-Württemberg. This collaboration has also benefited from support by the European Union's Horizon 2020 Research and Innovation Program under the Marie Skłodowska-Curie Grant Agreement No. 734557.

## DATA AVAILABILITY

The data that support the findings of this study are available from the corresponding author upon reasonable request.

## REFERENCES

- H. Eyring, J. Chem. Phys. **3**, 107 (1935), doi:10.1063/1.1749604.
- E. P. Wigner, J. Chem. Phys. **5**, 720 (1937), doi:10.1063/1.1750107.
- E. Pollak, M. S. Child, and P. Pechukas, J. Chem. Phys. **72**, 1669 (1980), doi:10.1063/1.439276.
- P. Pechukas, Annu. Rev. Phys. Chem. **32**, 159 (1981), doi:10.1146/annurev.pc.32.100181.001111.
- D. G. Truhlar, B. C. Garrett, and S. J. Klippenstein, J. Phys. Chem. **100**, 12771 (1996), doi:10.1021/jp953748q.
- B. K. Carpenter, "Potential energy surfaces and reaction dynamics," in *Reactive Intermediate Chemistry* (John Wiley & Sons, Ltd, 2005) Chap. 21, pp. 925–960.
- R. G. Mullen, J.-E. Shea, and B. Peters, J. Chem. Phys. **140**, 041104 (2014), doi:10.1063/1.4862504.

- <sup>8</sup>S. Arrhenius, *Z. Phys. Chem. (Leipzig)* **4**, 226 (1889), translated and published in Margaret H. Back and Keith J. Laidler, eds., *Selected Readings in Chemical Kinetics* (Oxford: Pergamon, 1967).
- <sup>9</sup>K. J. Laidler, *J. Chem. Educ.* **61**, 494 (1984), doi:10.1021/ed061p494.
- <sup>10</sup>E. Pollak, *J. Chem. Phys.* **93**, 1116 (1990), doi:10.1063/1.459175.
- <sup>11</sup>E. Pollak, in *Dynamics of Molecules and Chemical Reactions*, edited by R. E. Wyatt and J. Zhang (Marcel Dekker, New York, 1996) pp. 617–669.
- <sup>12</sup>T. Uzer, C. Jaffé, J. Palacián, P. Yanguas, and S. Wiggins, *Nonlinearity* **15**, 957 (2002), doi:10.1088/0951-7715/15/4/301.
- <sup>13</sup>T. Komatsuzaki and R. S. Berry, *Proc. Natl. Acad. Sci. U.S.A.* **98**, 7666 (2001), doi:10.1073/pnas.131627698.
- <sup>14</sup>T. Komatsuzaki and R. S. Berry, *Adv. Chem. Phys.* **123**, 79 (2002), doi:10.1002/0471231509.ch2.
- <sup>15</sup>T. Bartsch, R. Hernandez, and T. Uzer, *Phys. Rev. Lett.* **95**, 058301 (2005), doi:10.1103/PhysRevLett.95.058301.
- <sup>16</sup>E. Pollak and P. Talkner, *Chaos* **15**, 026116 (2005), doi:10.1063/1.1858782.
- <sup>17</sup>T. Bartsch, J. M. Moix, R. Hernandez, S. Kawai, and T. Uzer, *Adv. Chem. Phys.* **140**, 191 (2008), doi:10.1002/9780470371572.ch4.
- <sup>18</sup>R. Hernandez, T. Bartsch, and T. Uzer, *Chem. Phys.* **370**, 270 (2010), doi:10.1016/j.chemphys.2010.01.016.
- <sup>19</sup>H. Waalkens, R. Schubert, and S. Wiggins, *Nonlinearity* **21**, R1 (2008), doi:10.1088/0951-7715/21/1/R01.
- <sup>20</sup>S. Wiggins, *Regul. Chaotic Dyn.* **21**, 621 (2016), doi:10.1134/S1560354716060034.
- <sup>21</sup>G. S. Ezra, H. Waalkens, and S. Wiggins, *J. Chem. Phys.* **130**, 164118 (2009), doi:10.1063/1.3119365.
- <sup>22</sup>N. Fenichel, *Indiana Univ. Math. J.* **21**, 193 (1972), doi:10.1512/iumj.1972.21.21017.
- <sup>23</sup>S. Wiggins, *Normally Hyperbolic Invariant Manifolds in Dynamical Systems* (Springer, New York, 1994).
- <sup>24</sup>M. Feldmaier, A. Junginger, J. Main, G. Wunner, and R. Hernandez, *Chem. Phys. Lett.* **687**, 194 (2017), doi:10.1016/j.cplett.2017.09.008.
- <sup>25</sup>M. Feldmaier, P. Schraft, R. Bardakcioglu, J. Reiff, M. Lober, M. Tschöpe, A. Junginger, J. Main, T. Bartsch, and R. Hernandez, *J. Phys. Chem. B* **123**, 2070 (2019), doi:10.1021/acs.jpcc.8b10541.
- <sup>26</sup>E. Pollak and P. Pechukas, *J. Chem. Phys.* **69**, 1218 (1978), doi:10.1063/1.436658.
- <sup>27</sup>P. Pechukas and E. Pollak, *J. Chem. Phys.* **71**, 2062 (1979), doi:10.1063/1.438575.
- <sup>28</sup>R. Hernandez and W. H. Miller, *Chem. Phys. Lett.* **214**, 129 (1993), doi:10.1016/0009-2614(93)90071-8.
- <sup>29</sup>R. Hernandez, *J. Chem. Phys.* **101**, 9534 (1994), doi:10.1063/1.467985.
- <sup>30</sup>S. Wiggins, L. Wiesenfeld, C. Jaffe, and T. Uzer, *Phys. Rev. Lett.* **86** (2001), doi:10.1103/PhysRevLett.86.5478.
- <sup>31</sup>C. Jaffé, S. D. Ross, M. W. Lo, J. Marsden, D. Farrelly, and T. Uzer, *Phys. Rev. Lett.* **89**, 011101 (2002), doi:10.1103/PhysRevLett.89.011101.
- <sup>32</sup>H. Teramoto, M. Toda, and T. Komatsuzaki, *Phys. Rev. Lett.* **106**, 054101 (2011), doi:10.1103/PhysRevLett.106.054101.
- <sup>33</sup>C.-B. Li, A. Shoujiguchi, M. Toda, and T. Komatsuzaki, *Phys. Rev. Lett.* **97**, 028302 (2006), doi:10.1103/PhysRevLett.97.028302.
- <sup>34</sup>H. Waalkens and S. Wiggins, *J. Phys. A* **37**, L435 (2004), doi:10.1088/0305-4470/37/35/L02.
- <sup>35</sup>U. Çiftçi and H. Waalkens, *Phys. Rev. Lett.* **110**, 233201 (2013), doi:10.1103/PhysRevLett.110.233201.
- <sup>36</sup>A. M. Mancho, D. Small, S. Wiggins, and K. Ide, *Physica D* **182**, 188 (2003), doi:10.1016/S0167-2789(03)00152-0.
- <sup>37</sup>G. T. Craven and R. Hernandez, *Phys. Rev. Lett.* **115**, 148301 (2015), doi:10.1103/PhysRevLett.115.148301.
- <sup>38</sup>C. Lopesino, F. Balibrea-Iniesta, V. J. García-Garrido, S. Wiggins, and A. M. Mancho, *Int. J. Bifurc. Chaos* **27**, 1730001 (2017), doi:10.1142/S0218127417300014.
- <sup>39</sup>R. Bardakcioglu, A. Junginger, M. Feldmaier, J. Main, and R. Hernandez, *Phys. Rev. E* **98**, 032204 (2018), doi:10.1103/PhysRevE.98.032204.
- <sup>40</sup>P. Schraft, A. Junginger, M. Feldmaier, R. Bardakcioglu, J. Main, G. Wunner, and R. Hernandez, *Phys. Rev. E* **97**, 042309 (2018), doi:10.1103/PhysRevE.97.042309.
- <sup>41</sup>M. Tschöpe, M. Feldmaier, J. Main, and R. Hernandez, *Phys. Rev. E* **101**, 022219 (2020), doi:10.1103/PhysRevE.101.022219.
- <sup>42</sup>F. Revuelta, G. T. Craven, T. Bartsch, F. Borondo, R. M. Benito, and R. Hernandez, *J. Chem. Phys.* **147**, 074104 (2017), doi:10.1063/1.4997571.
- <sup>43</sup>T. Bartsch, F. Revuelta, R. M. Benito, and F. Borondo, *Phys. Rev. E* **99**, 052211 (2019), doi:10.1103/PhysRevE.99.052211.
- <sup>44</sup>M. Feldmaier, R. Bardakcioglu, J. Reiff, J. Main, and R. Hernandez, *J. Chem. Phys.* **151**, 244108 (2019), doi:10.1063/1.5127539.
- <sup>45</sup>G. T. Craven, T. Bartsch, and R. Hernandez, *J. Chem. Phys.* **141**, 041106 (2014), doi:10.1063/1.4891471.
- <sup>46</sup>T. Bartsch, T. Uzer, and R. Hernandez, *J. Chem. Phys.* **123**, 204102 (2005), doi:10.1063/1.2109827.
- <sup>47</sup>D. G. Truhlar, A. D. Isaacson, R. T. Skodje, and B. C. Garrett, *J. Phys. Chem.* **86**, 2252 (1982), doi:10.1021/j100209a021.
- <sup>48</sup>E. Pollak, in *Theoretical Methods in Condensed Phase Chemistry*, edited by S. D. Schwartz (Kluwer Academic Publishers, Dordrecht, 2000) pp. 1–46.
- <sup>49</sup>J. H. Araban, P. B. Changala, G. C. Mellau, J. F. Stanton, A. J. Merer, and R. W. Field, *Science* **350**, 1338 (2015), doi:10.1126/science.aac9668.
- <sup>50</sup>H. Waalkens, A. Burbanks, and S. Wiggins, *J. Chem. Phys.* **121**, 6207 (2004).
- <sup>51</sup>A. B. McCoy and E. L. Sibert III, *J. Chem. Phys.* **95**, 3476 (1991), doi:10.1063/1.460851.
- <sup>52</sup>R. Essers, J. Tennyson, and P. E. S. Wormer, *Chem. Phys. Lett.* **89**, 223 (1982), doi:10.1016/0009-2614(82)80046-8.
- <sup>53</sup>G. Brocks, J. Tennyson, and A. van der Avoird, *J. Chem. Phys.* **80**, 3223 (1984), doi:10.1063/1.447075.
- <sup>54</sup>P. L. García-Müller, F. Borondo, R. Hernandez, and R. M. Benito, *Phys. Rev. Lett.* **101**, 178302 (2008), doi:10.1103/PhysRevLett.101.178302.
- <sup>55</sup>P. L. García-Müller, R. Hernandez, R. M. Benito, and F. Borondo, *J. Chem. Phys.* **137**, 204301 (2012), doi:10.1063/1.4766257.
- <sup>56</sup>P. L. García-Müller, R. Hernandez, R. M. Benito, and F. Borondo, *J. Chem. Phys.* **141**, 074312 (2014), doi:10.1063/1.4892921.
- <sup>57</sup>A. Junginger, P. L. García-Müller, F. Borondo, R. M. Benito, and R. Hernandez, *J. Chem. Phys.* **144**, 024104 (2016), doi:10.1063/1.4939480.
- <sup>58</sup>A. Vergel, R. M. Benito, J. C. Losada, and F. Borondo, *Phys. Rev. E* **89**, 022901 (2014), doi:10.1103/PhysRevE.89.022901.
- <sup>59</sup>S. D. Prado, E. G. Vergini, R. M. Benito, and F. Borondo, *Europhys. Lett.* **88**, 40003 (2009), doi:10.1209/0295-5075/88/40003.
- <sup>60</sup>G. E. Murgida, D. A. Wisniacki, P. I. Tamborenea, and F. Borondo, *Chem. Phys. Lett.* **496**, 356 (2010), doi:10.1016/j.cplett.2010.07.057.
- <sup>61</sup>F. Revuelta, R. Chacón, and F. Borondo, *Europhys. Lett.* **110**, 40007 (2015), doi:10.1209/0295-5075/110/40007.
- <sup>62</sup>G. E. Murgida, F. J. Arranz, and F. Borondo, *J. Chem. Phys.* **143**, 214305 (2015), doi:10.1063/1.4936424.
- <sup>63</sup>G. Brocks and J. Tennyson, *J. Mol. Spectrosc.* **99**, 263 (1983).
- <sup>64</sup>P. E. S. Wormer and J. Tennyson, *J. Chem. Phys.* **75**, 1245 (1981), doi:10.1063/1.442174.
- <sup>65</sup>R. Benito, F. Borondo, J.-H. Kim, B. Sumpter, and G. Ezra, *Chem. Phys. Lett.* **161**, 60 (1989), doi:10.1016/S0009-2614(89)87032-0.
- <sup>66</sup>W. H. Press, S. A. Teukolsky, W. T. Vetterling, and B. P. Flannery, *Numerical recipes: The art of scientific computing* (Cambridge University Press, New York, 1987).
- <sup>67</sup>Throughout the paper, we use atomic units—Bohr radius  $a_0$ , elementary charge  $e$ , and  $1 E_h$  (Hartree)—for length, charge, and energy, but 1 u (dalton) as the mass unit. As a consequence, times

must be multiplied and frequencies and rates must be divided by a factor of  $\sqrt{1 \text{ u}/m_e} = \sqrt{1823} = 42.7$  to obtain the corresponding values in atomic units.

<sup>68</sup>J. D. Jackson, *Classical electrodynamics* (John Wiley & Sons, 2012).

<sup>69</sup>These values have been updated to reflect a correction due to the unit conversion noted in footnote 67.

<sup>70</sup>S. Wimberger, *Nonlinear dynamics and quantum chaos* (Springer, Cham, 2014).

<sup>71</sup>F. Revuelta, R. M. Benito, and F. Borondo, Phys. Rev. E **99**, 032221 (2019), doi:10.1103/PhysRevE.99.032221.



for the computation of the decay rates of reactant populations of multidimensional driven systems with a rank-1 saddle—*viz.* the ensemble method, the local manifold analysis (LMA), and the Floquet method. For the convenience of the reader we briefly recapitulate the basic ideas of these methods, which are then applied in the results section to the LiCN isomerization reaction.

### A. Floquet method for average decay rates

Reaction rates of the TS in a one-dimensional system had earlier been obtained directly from the moving TS trajectory through its stability exponents.<sup>6,7</sup> The latter correspond to Floquet exponents in a periodically driven system,<sup>6</sup> and Lyapunov exponents in nonperiodic driving.<sup>7</sup> In these early examples, the decay rates associated with the TS trajectory were identifiable as reaction rates because the local TS geometry was actually global in the sense of identifying long-time reactivity and global non-recrossing. However, for more general energy landscapes, the determination of the TS trajectory in 1-dimension or its generalizations may be local in the sense of being obtained within a limited domain associated with a barrier (or barriers.) This is the sense in which we are obtaining local decay rates and not necessarily global reaction rates in this work. Thus, the stability of the TS trajectory obtained within a given local region is associated with the so-called Floquet rate which uses the Floquet exponents to obtain the reaction rate when the local geometry is global.

In multidimensional cases, one has to take care of the fact that the TS trajectory becomes a time-dependent codimension-2 manifold—*viz.* the NHIM—associated with infinitely many trajectories which we refer to as bound trajectories.<sup>4,8</sup> For periodically driven arbitrary-dimensional systems, the decay rates (or Floquet rates), are simply obtained by the difference

$$k_F = \mu_l - \mu_s, \quad (1)$$

between a Floquet exponent  $\mu_l$  associated with the unstable direction of trajectories moving away from the NHIM, and a Floquet exponent  $\mu_s$  associated with the stable motion of the trajectories towards the NHIM. In 1-dimension, there are only two such exponents, and hence there is only one choice for  $\mu_l$  and  $\mu_s$ .<sup>6</sup> In general, however, there are many such exponents and infinitely many bound trajectories. Nevertheless, the structure of Eq. (1) holds as specified below.

The Floquet exponents are a measure of how exponentially fast initially neighboring trajectories separate from each other.<sup>9</sup> Consequently, they report the stability of these trajectories. The dynamics in the direction of the  $n - 1$  orthogonal modes of a rank-1 saddle is *stable*. Initially neighboring trajectories do not separate exponentially fast as they are propagated with respect to these stable degrees of freedom—as long as the dynamics inside the NHIM is not chaotic. Consequently, the

corresponding Floquet exponents vanish and the related eigenvalues of the monodromy matrix have an absolute value of one. In the unstable direction of a rank-1 barrier, however, initially neighboring trajectories will depart exponentially fast at least in a local neighborhood of the NHIM and, hence, the associated Floquet exponents do not vanish. For a periodic trajectory with period  $T$  on the NHIM, these non-vanishing Floquet exponents are obtained from

$$\mu_{l,s} = \frac{1}{T} \ln |m_{l,s}|. \quad (2)$$

Here,  $m_l$  is the largest and  $m_s$  is the smallest eigenvalue of the corresponding monodromy matrix  $\mathbf{M}(T)$ , and this specifies precisely the meaning of the two chosen Floquet exponents in Eq. (1). The monodromy matrix  $\mathbf{M}(T) = \boldsymbol{\sigma}(t_0 + T, t_0)$  is a special case of the fundamental matrix  $\boldsymbol{\sigma}(t, t_0)$ , which is obtained by solving the set of differential equations

$$\frac{d}{dt} \boldsymbol{\sigma}(t, t_0) = \left. \frac{\partial \dot{\gamma}_i}{\partial \gamma_j} \right|_{\boldsymbol{\gamma}(t)} \boldsymbol{\sigma}(t, t_0) \text{ with } \boldsymbol{\sigma}(t_0, t_0) = \mathbb{1}. \quad (3)$$

Here,  $\dot{\boldsymbol{\gamma}}$  are the  $(2n)$ -dimensional equations of motion in phase space and  $\boldsymbol{\gamma}(t)$  is a trajectory on the NHIM. Since the Floquet exponents are obtained for a full period of the external driving according to Eqs. (2), the Floquet rate (1) is an integrated quantity corresponding to a mean decay rate averaged over a full periodic trajectory.

According to Ref. 4, only a small set (of measure zero) of trajectories on the NHIM of a periodically driven system are periodic, but nearly all of them do show quasi-periodic behavior as long as the dynamics in the orthogonal modes is not chaotic. For these quasi-periodic trajectories inside the NHIM, Eq. (2) needs to be modified as

$$\mu_{l,s} = \lim_{t \rightarrow \infty} \frac{1}{t} \ln |m_{l,s}(t)| \quad (4)$$

to obtain the Floquet exponents associated with a specific torus on the NHIM. Since the calculation of the infinite time limit in Eq. (4) is numerically impossible, the integration time  $t$  must, in practice, be taken to be sufficiently large to cover the relevant or characteristic dynamics of the observed trajectory—e.g., long enough to traverse several windings on a stable torus. In doing so, the Floquet rate of such a quasi-periodic trajectory corresponds to the mean decay rate of the reactant population close to the respective torus.

### B. Ensemble method for instantaneous decay rates

The ensemble method is an intuitive numerical method for obtaining the instantaneous decay rate of a reactant population close to the TS. Here, a homogeneous and linear ensemble of  $N_{\text{react}}$  reactive trajectories is initialized on the reactant side of the full phase space.

Specifically, they are placed on an  $(x, p_x)$ -cross sectional surface at a small distance  $\Delta x$  from a given position  $(\mathbf{y}^{\text{traj}}(t), \mathbf{p}_y^{\text{traj}}(t))$  of an arbitrarily chosen trajectory on the NHIM (see red bullets in Fig. 1). After propagating this ensemble for a time  $\Delta t$ , a subdomain will have pierced the DS and entered the product side (dark blue diamonds and light blue squares in Fig. 1) while the remainder will still be located on the reactant side (red stars in Fig. 1). As the DS is non-recrossing, the resulting decrease in the reactant population of a close neighborhood of the NHIM is associated with a rate

$$k_e(\mathbf{y}, \mathbf{p}_y, t) = -\frac{d}{dt} \ln(N_{\text{react}}(\mathbf{y}, \mathbf{p}_y, t)). \quad (5)$$

It is referred to as the *instantaneous ensemble rate* to emphasize that it is obtained by propagating an ensemble of reactive trajectories according to the equations of motion. In doing so, the DS is computed individually for each trajectory of the ensemble and each time step.

The ensemble can be propagated not just for a small time step  $\Delta t$  but for longer times when computing the time-dependent ensemble rate according to Eq. (5). With increasing time, however, the initial ensemble becomes more and more distorted (see Sec. IIC for further information). Since the DS is computed individually for each reactive trajectory, such distortion effects are automatically taken into account using the ensemble method. As the reactant population also decreases exponentially when propagating the ensemble, a new ensemble can be initialized close to the corresponding point of the respective trajectory on the NHIM after an appropriately chosen propagation time. Such technical details are discussed in Ref. 4. Although the implementation of the ensemble method is straightforward, it can be numerically expensive because the ensemble consists of many trajectories and the DS is obtained individually for each reactive trajectory using the BCM.<sup>3</sup>

### C. Local manifold analysis

We can avoid most of the expensive particle propagation of the ensemble method by leveraging the geometry of the stable and unstable manifolds to effectively describe the linearized dynamics near the NHIM. The resulting LMA method<sup>4</sup> can thus be seen as an extension to the ensemble method with the difference that the time when trajectories have reached the DS can now be determined analytically through the linearization thereby avoiding a costly numerical integration. As a result, the computational effort required to calculate instantaneous decay rates is significantly reduced while numerical precision is simultaneously enhanced.

Similar to the ensemble method, in the LMA, we consider the region of phase space close to a trajectory  $\gamma^\ddagger = (x^\ddagger, \mathbf{y}^\ddagger, p_x^\ddagger, \mathbf{p}_y^\ddagger)^\top$  on the NHIM, as shown in Fig. 1. For simplicity, we choose a moving coordinate frame in which the origin is at  $x^\ddagger = p_x^\ddagger = 0$  for all times  $t$ .

The decay rate is determined by two components:

(i) The first contribution arises from the movement of the ensemble akin to Sec. IIB relative to  $\gamma^\ddagger$ . The resulting flux through the associated DS at  $x^{\text{DS}} = 0$  (dark blue diamonds in Fig. 1) is then obtained via the slopes of the stable and unstable manifolds defined by the variables  $x^s = x^u$ ,  $p_x^s$ , and  $p_x^u$ . The details and mathematical underpinnings of this procedure, based on Ref. 4, may be found in Sec. III.

(ii) The second contribution accounts for the fact that in systems with more than one degree of freedom, the ensemble can turn out of the  $(x, p_x)$  plane associated with  $\gamma^\ddagger$ . This can happen if the system's orthogonal modes are coupled to the reaction coordinate momentum  $p_x$  and leads to an apparent movement of the DS relative to  $\gamma^\ddagger$  (represented by  $\Delta x^{\text{DS}}$  and bright blue diamonds in Fig. 1). As a result, the instantaneous flux through the DS is modified. To quantify this effect, we first propagate the top particle of the ensemble initially located on the DS numerically by a small time step  $\delta t$ . The related shift of the DS,  $x^{\text{DS}}(t + \delta t)$ , can then be determined by projecting the propagated particle back onto the NHIM using the BCM.

Combining the two terms, the instantaneous decay rate can be written as

$$k_m(t; \gamma^\ddagger) = \mathbf{J}_{x, p_x}(t) \frac{p_x^u(t) - p_x^s(t)}{x^u(t)} - \frac{x^{\text{DS}}(t + \delta t)}{x^u(t) \delta t}, \quad (6)$$

where  $\mathbf{J}(t)$  is the Jacobian of the system's equations of motion evaluated for the trajectory  $\gamma^\ddagger$  at time  $t$ . A more detailed derivation of Eq. (6) is provided in Sec. III

## III. DERIVATION OF THE LOCAL MANIFOLD ANALYSIS

We consider a trajectory  $\gamma^\ddagger(t) = (x^\ddagger, \mathbf{y}^\ddagger, p_x^\ddagger, \mathbf{p}_y^\ddagger)^\top$  starting at some arbitrary time  $t_0$  on the normally hyperbolic invariant manifold (NHIM). All of the statements in this section depend implicitly on  $\gamma^\ddagger$  and  $t_0$ , which we neglect in our notation for simplicity. Without loss of generality, we choose coordinates such that  $x^\ddagger(t) = p_x^\ddagger(t) = 0$  for all times  $t$ . Figure 1 sketches an  $(x, p_x)$ -section of phase space in close proximity to  $\gamma^\ddagger(t_0)$ . We can assume that the manifold fibers in this section are straight lines since we only look at the dynamics very close to the NHIM. Therefore, the stable and unstable manifolds can be described using only two vectors  $\gamma^s = (x^s, p_x^s)^\top$  and  $\gamma^u = (x^u, p_x^u)^\top$ . These vectors will be squeezed and stretched as a function of time if subjected to the equations of motion. Without loss of generality, we initially choose  $0 < x^s(t_0) = x^u(t_0)$  such that we are in the linear regime.

To obtain a decay rate for  $\gamma^\ddagger(t_0)$ , we now consider a linear, equidistant ensemble parameterized by

$$\gamma^{\text{ens}}(a, t) = -\gamma^s(t) + a\gamma^u(t) \quad (7)$$



where  $a \in [0, 1]$ . The ensemble is constructed parallel to the unstable manifold—see Fig. 1. Initially, the ensemble pierces the dividing surface (DS) at  $a^{\text{DS}}(t_0) = 1$  (circles in Fig. 1). As time goes by, however, the ensemble will be stretched and  $a^{\text{DS}}(t)$  will therefore decay exponentially (diamonds in Fig. 1). More precisely,  $a^{\text{DS}}$  is proportional to the number of reactants and therefore leads to a decay rate

$$k_{\text{m}}(t_0) = - \left. \frac{d}{dt} \ln(a^{\text{DS}}(t)) \right|_{t_0} = -\dot{a}^{\text{DS}}(t_0) \quad (8)$$

at time  $t_0$  in analogy to Eq. (5). In this picture, the total decay rate consists of two contributions

$$k_{\text{m}}(t_0) = k^{\text{ens}}(t_0) + k^{\text{DS}}(t_0). \quad (9)$$

For the first part,  $k^{\text{ens}}$ , we assume that the ensemble stays in the  $(x, p_x)$ -section associated with  $\gamma^\ddagger(t)$ . As a result, the point where the ensemble pierces the DS is fixed at  $x^{\text{DS}}(t) = 0$  for all times  $t$ . This is an effectively one-dimensional model. We start by looking at the linearized dynamics near the NHIM

$$\frac{d}{dt} \gamma(t) = \mathbf{J}(t) \gamma(t), \quad (10)$$

where  $\mathbf{J}(t)$  is the Jacobian of the system's equations of motion evaluated on the trajectory  $\gamma^\ddagger$ . The fundamental matrix  $\sigma(t)$  obtained by integrating  $\dot{\sigma}(t) = \mathbf{J}(t)\sigma(t)$  with  $\sigma(t_0) = \mathbb{1}$  [cf. Eq. (3)] can then be used to propagate the ensemble from time  $t_0$  to a later time  $t$  via

$$\gamma^{\text{ens}}(a, t) = \sigma(t) \gamma^{\text{ens}}(a, t_0). \quad (11)$$

We are interested in the point  $a^{\text{DS}}$  where  $\gamma^{\text{ens}}(a, t)$  pierces the DS at  $x^{\text{DS}}(t) = 0$ , i. e.,

$$\sigma(t) \gamma^{\text{ens}}(a^{\text{DS}}(t), t_0) \cdot \hat{\mathbf{e}}_x \stackrel{!}{=} 0. \quad (12)$$

Inserting Eq. (7) yields

$$a^{\text{DS}}(t) = \frac{\sigma_{x,x}(t)x^{\text{u}}(t_0) + \sigma_{x,p_x}(t)p_x^{\text{s}}(t_0)}{\sigma_{x,x}(t)x^{\text{u}}(t_0) + \sigma_{x,p_x}(t)p_x^{\text{u}}(t_0)}, \quad (13)$$

where we have used  $x^{\text{s}}(t_0) = x^{\text{u}}(t_0)$ . This intermediate result can be substituted into Eq. (8). Since we are only interested in the instantaneous rate at  $t = t_0$ , we can simplify the expression using  $\sigma(t_0) = \mathbb{1}$  as well as  $\dot{\sigma}_{x,p_x}(t_0) = \mathbf{J}_{x,p_x}(t_0)$  and arrive at

$$k^{\text{ens}}(t_0) = \mathbf{J}_{x,p_x} \frac{p_x^{\text{u}}(t_0) - p_x^{\text{s}}(t_0)}{x^{\text{u}}(t_0)}. \quad (14)$$

A geometric interpretation of  $k^{\text{ens}}$  can be found in Ref. 4.

The second contribution,  $k^{\text{DS}}$ , in Eq. (9) stems from the fact that in systems with more than one degree of freedom the ensemble may leave the  $(x, p_x)$ -section associated with  $\gamma^\ddagger(t)$ . An ensemble moving out-of-plane can mostly be treated as described above by projecting it back onto the  $(x, p_x)$ -section. Since the position of the DS  $x^{\text{DS}}(\mathbf{y}, \mathbf{p}_y)$  is dependent on the orthogonal modes, however, this may lead to the ensemble intersecting with the DS at  $x^{\text{DS}} \neq 0$ .

To quantify the effect on  $k_{\text{m}}$ , consider a small time step  $\delta t$ . In the linear regime, the change  $\delta a$  caused by the ensemble drifting out-of-plane can be written as

$$\delta a^{\text{DS}}(t_0) = \frac{x^{\text{DS}}(t_0 + \delta t) - x^{\text{DS}}(t_0)}{x^{\text{u}}(t_0)}, \quad (15)$$

where  $x^{\text{u}}(t_0)$  accounts for normalization. Using Eq. (8) and the fact that  $x^{\text{DS}}(t_0) = 0$ , we obtain

$$k^{\text{DS}}(t_0) = - \frac{\delta a^{\text{DS}}(t_0)}{\delta t} = - \frac{x^{\text{DS}}(t_0 + \delta t)}{x^{\text{u}}(t_0) \delta t}. \quad (16)$$

The quantities  $\delta t$  and  $x^{\text{u}}$  can be freely chosen within certain limits, while  $x^{\text{DS}}(t_0 + \delta t)$  can be determined numerically by propagating the particle  $\gamma^{\text{ens}}(1, t_0)$  initially located on the DS for  $\delta t$  units of time and projecting it back onto the NHIM using the binary contraction method (BCM).<sup>3</sup> By combining Eqs. (14) and (16) according to Eq. (9), we finally arrive at the instantaneous decay rate  $k_{\text{m}}(t; \gamma^\ddagger)$  for a trajectory  $\gamma^\ddagger$  on the NHIM given in Eq. (6) of Sec. IIC.

## REFERENCES

- <sup>1</sup>A. Junginger, L. Duvenbeck, M. Feldmaier, J. Main, G. Wunner, and R. Hernandez, *J. Chem. Phys.* **147**, 064101 (2017).
- <sup>2</sup>M. Feldmaier, P. Schraft, R. Bardakcioglu, J. Reiff, M. Lober, M. Tschöpe, A. Junginger, J. Main, T. Bartsch, and R. Hernandez, *J. Phys. Chem. B* **123**, 2070 (2019).
- <sup>3</sup>R. Bardakcioglu, A. Junginger, M. Feldmaier, J. Main, and R. Hernandez, *Phys. Rev. E* **98**, 032204 (2018).
- <sup>4</sup>M. Feldmaier, R. Bardakcioglu, J. Reiff, J. Main, and R. Hernandez, *J. Chem. Phys.* **151**, 244108 (2019).
- <sup>5</sup>P. Schraft, A. Junginger, M. Feldmaier, R. Bardakcioglu, J. Main, G. Wunner, and R. Hernandez, *Phys. Rev. E* **97**, 042309 (2018).
- <sup>6</sup>G. T. Craven, T. Bartsch, and R. Hernandez, *J. Chem. Phys.* **141**, 041106 (2014).
- <sup>7</sup>F. Revuelta, G. T. Craven, T. Bartsch, F. Borondo, R. M. Benito, and R. Hernandez, *J. Chem. Phys.* **147**, 074104 (2017).
- <sup>8</sup>M. Tschöpe, M. Feldmaier, J. Main, and R. Hernandez, *Phys. Rev. E* **101**, 022219 (2020).
- <sup>9</sup>H. Goldstein, *Classical Mechanics*, Addison-Wesley Series in Physics (Addison-Wesley, London, 1980).